

Cite this: DOI: 00.0000/xxxxxxxxxx

Viscoelasticity and elastocapillarity effects in the impact of drops on a repellent surface[†]

Carole-Ann Charles,^a Ameer Louhichi,^a Laurence Ramos,^a and Christian Liguore^{* a}

Received Date
Accepted Date

DOI: 00.0000/xxxxxxxxxx

We investigate freely expanding viscoelastic sheets. The sheets are produced by the impact of drops on a quartz plate covered with a thin layer of liquid nitrogen that suppresses shear viscous dissipation as a result of the cold Leidenfrost effect. The time evolution of the sheet is simultaneously recorded from top and side views using high-speed cameras. The investigated viscoelastic fluids are Maxwell fluids, which are characterized by low elastic moduli, and relaxation times that vary over almost two orders of magnitude, thus giving access to a large spectrum of viscoelastic and elastocapillary effects. For the purposes of comparison, Newtonian fluids, with viscosity varying over three orders of magnitude, are also investigated. In this study, d_{\max} , the maximal expansion of the sheets, and t_{\max} the time to reach this maximal expansion from the time at impact, are measured as a function of the impact velocity. By using a generalized damped harmonic oscillator model, we rationalize the role of capillarity, bulk elasticity and viscous dissipation in the expansion dynamics of all investigated samples. In the model, the spring constant is a combination of the surface tension and the bulk dynamic elastic modulus. The time-varying damping coefficient is associated to biaxial extensional viscous dissipation and is proportional to the dynamic loss modulus. For all samples, we find that the model reproduces accurately the experimental data for d_{\max} and t_{\max} .

1 Introduction

When a drop with a high level of kinetic energy hits a surface, it expands radially into a transient sheet, until reaching a maximum diameter before, in some cases, receding partially or completely depending on the nature of the drop and the surface. Predicting the maximum diameter and the time needed for the sheet to reach the latter is crucial for many industrial applications such as spray coating¹, pesticide application², forensic science³ or ink-jet printing⁴. As a matter of fact, the dynamics of drop impact has been extensively studied over the years and has been greatly aided by the emergence of high speed imaging^{5,6}. The impact of a drop can now be observed in real time for various systems such as Newtonian fluids with different viscosities^{7,8}, suspensions of particles^{9,10}, shear thickening fluids¹¹, polymer solutions¹² or other viscoelastic materials¹³ as well as soft elastic beads¹⁴. These materials are impacted on many different surfaces such as thick and thin liquid films or solid surfaces of different roughness¹⁵ and wettability¹⁶ but also of different sizes, geometries^{6,7,17} or inclinations¹⁸.

Numerous rationalizations⁶ and simulations^{19–21} of the impact process have provided great insight into the expansion dynamics of Newtonian fluids. These models are generally based on a balance of energy and aim to predict the maximum diameter reached by the sheet as a function of characteristic adimensional numbers (Reynolds, Weber and Ohnesorge numbers). In the case of viscoelastic fluids, rationalization is however more complex and was not as extensively studied^{22,23}. Though, because most industrial impact phenomenon involve viscoelastic fluids, understanding the behavior of impacted viscoelastic drops is of great interest.

Impact dynamics of viscoelastic fluids is more complex than for Newtonian fluids. For this reason, we simplify the contribution of dissipation by impacting drops on a repellent surface. Such surfaces include superhydrophobic surfaces²⁴, hot plates above the Leidenfrost temperature^{25,26} or cold plates used in cold Leidenfrost conditions^{14,27}. Repellent surfaces avoid a direct contact between the liquid sheet and the solid surface hence it suppresses the contact between the drop and the solid surface during drop collision and sheet expansion. Viscous dissipation due to shear is therefore suppressed. However, the use of repellent surfaces does not suppress all viscous dissipation. We have recently shown that biaxial extensional viscosity is the relevant source of viscous dissipation involved in the impact dynamics of drops in cold Leidenfrost conditions for which the shear dissipation is suppressed²⁸.

^a Laboratoire Charles Coulomb (L2C), Université de Montpellier, CNRS, Montpellier, France

[†] Electronic Supplementary Information (ESI) available: [details of any supplementary information available should be included here]. See DOI: 10.1039/cXsm00000x/

^{*} Corresponding author: christian.liguore@umontpellier.fr

In this work, we investigate the expansion dynamics of freely expanding sheets formed by the impact of drops of viscoelastic fluids for which the effects of bulk elasticity, capillarity and viscosity combine in a non trivial way. Drops are impacted in cold Leidenfrost conditions at several impact velocities. A simple model of 1D harmonic oscillator was used to provide a quantitative estimate of the expansion dynamics of sheets without viscous dissipation for drops of inviscid fluids^{29,30}, for elastic beads³¹ and for ultra soft elastic beads and viscoelastic drops with long relaxation times with respect to the duration of the impact experiment¹⁴. Viscous damping has also been recently included in the 1D oscillator model to account for viscous dissipation in the rebound of Newtonian fluids³² or droplet oscillation after impact³³. Here, we show that taking into account the viscoelastic nature of the samples is crucial to capture into a generalized damped oscillator model, beyond the scaling arguments, the non-trivial combination of bulk elasticity, surface tension and viscosity in the expansion dynamics of viscoelastic drops following impact. The model successfully describes the expansion of sheets made from viscoelastic fluids as well as Newtonian liquids with a wide range of viscosities allowing one to extend investigations further than the capillary regime.

2 Methods and materials

2.1 Experimental set-up

With the aim of weeding out the shear dissipation, drop impact experiments are performed under cold Leidenfrost conditions using a set-up described previously^{14,28}. The drop at ambient temperature impacts a quartz plate covered by a thin layer of liquid nitrogen (boiling point $T_s = -196.15^\circ\text{C}$). As the temperature of the drop is higher than T_s , the liquid nitrogen evaporates partially upon impact, creating a vapor layer under the expanding drop of typical thickness $100\mu\text{m}$ ³⁴. The drop is supported by the evaporating nitrogen throughout the whole expansion process and is left to expand free of shear viscous dissipation^{27,35}.

The experimental set-up is schematically shown in figure 1a. The drops are released from a needle (internal diameter 2 mm) placed vertically above the quartz surface and connected, through a flexible Teflon tube, to a syringe pump set at a flow rate of 1 ml/min. The initial diameter of the drop, d_0 , varies between 3.1 and 3.8 mm depending on the fluids surface tension. The height, H , from which the drop is released into a free fall is varied between 11 cm and 131 cm in order to obtain impact velocities ranging between 1.5 and 5 m/s. Drops accumulate inertial energy throughout their fall until reaching the surface covered with the thin liquid nitrogen layer where they expand and reach a maximal expansion before retracting due to surface tension and stored elastic energy. During retraction, some droplets are eventually expelled from the rim. The whole process is captured from the top, at an angle of approximately 10° with the vertical plane, by a high speed camera, Phantom V 7:3, operating at 6700 fps with a resolution of 800×600 pixels² and, for most experiments, simultaneously from the side by a Phantom miro M310 operating at 3200 fps with a resolution of 1280×800 pixels². We use the side

imaging to check that the sheets are flat during the whole duration of the expansion. The top view imaging is used to quantify the expansion dynamic. Proper illumination for acquisition is provided by high-intensity backlights; Phlox HSC with a luminance of 98 cd/m^2 in the bottom and Phlox LLUB with a luminance of 20 cd/m^2 on the side. The temperature (20°C on average) of the room is systematically measured before each impact experiment to control the experimental conditions. Between each impact, the substrate is cleaned with ethanol. Figures 1b,c show top and side views of a viscoelastic sheet taken at its maximal expansion. The snapshots show that the sheet at maximal expansion has a near circular shape and lays almost flat on the nitrogen gas.

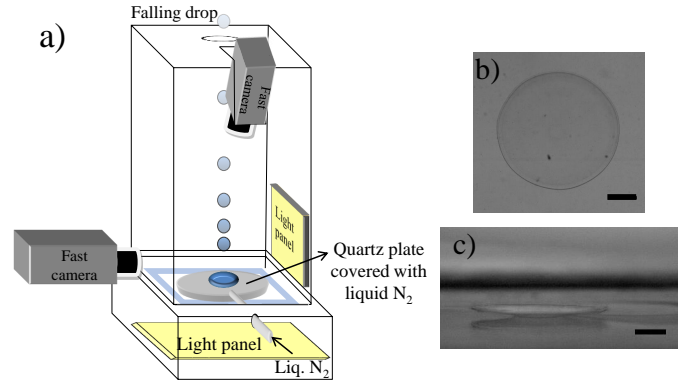


Fig. 1 (a) Schematic illustration of the set-up where a drop falls onto a quartz plate covered with a thin layer of liquid nitrogen. The impact is simultaneously recorded from the top and the side by two fast cameras. (b,c) Snapshots of a viscoelastic sheet (sample M14 ϕ 10r6) taken at maximal expansion from the top (b) and from the side (c). The impact velocity is $v_0 = 4.7\text{ m/s}$. The scale bars represent 5 mm.

As the temperature of the fluid on which the drop is impacted is very low ($T_s = -196.15^\circ\text{C}$, the boiling point of liquid nitrogen) as compared to the initial temperature of the drop (about 20°C), one should ensure that the drop does not freeze upon impact and that its temperature remains constant throughout the expansion. We thus quantify the typical time for the heat to transfer from the drop to the quartz plate and compare this time to the typical time of an experiment (typically of the order of a few ms). The principal heat transfer mode between the sample and the vapor layer is conduction^{36–38}. The calculation is reported in the supplementary materials †. It shows that the temperature of the sheet decreases by less than 0.8°C when the sheet reaches maximal expansion. Hence, it is reasonable to assume that the temperature of the sheet does not vary considerably until maximum expansion. Thus, in the following the rationalization of the experimental results will be done using the fluids properties measured at 20°C , close to the temperature of the drop impact experiments.

2.2 Image analysis

The stacks of frames obtained from top view imaging are analyzed using ImageJ software. The sheet is delimited by adjusting the threshold and its area, A , is measured for each frame using

the analyze particle command. We have checked that corrections in the measured area, due to the camera angle, can be safely neglected. An apparent diameter, d , is extracted using $d = \sqrt{\frac{4A}{\pi}}$. For Newtonian fluids with zero shear viscosities lower than 100 mPa s, the maximal diameter is corrected in accordance with observations made in Ref.²⁸. Indeed, for these low viscosity samples side view imaging shows that the sheet exhibits a corona shape, resulting in an underestimation of the actual diameter if simply estimated from top imaging²⁸. We check that for all investigated viscoelastic samples, the sheets remain flat and no correction is necessary. In the following, for each impact velocity and sample, the reported time evolution of the sheet diameter corresponds to an average over three different experiments.

2.3 Shear rheology

All samples are characterized rheologically using either Anton Paar MRC302 or ARES RFS 1KFRT rheometers, equipped with stainless steel cone and plate geometries of diameter 50 mm with an angle of 1° and a truncation of 101 μ m. Dynamic strain sweeps with strain amplitude from 0.1% to 100% are conducted at frequencies of 10 and 50 rad/s to define the linear viscoelastic regime. Dynamic frequency sweeps are performed at a strain amplitude $\gamma = 1\%$, well in the linear regime, for an angular frequency varying from 100 to 0.01 rad/s. Temperature is set at 20°C for all measurements and controlled using a Peltier element (accuracy of 0.2°C).

2.4 Systems

Two classes of fluids are investigated: two types of Newtonian liquids and two types of viscoelastic fluids.

The Newtonian liquids consist of silicone oil blends (SO) and glycerol-water mixtures (G-W). Silicone oils are purchased from Sigma Aldrich and blended to give mixtures of different viscosities. The zero shear viscosities of the blends vary from 5 mPa s to 970 mPa s as measured at 20°C, their average surface tension is 20 mN/m³⁹ and their density varies between 0.913 and 0.97 g/ml (as calculated from the densities of the purchased silicone oils). The composition of glycerol-water mixtures varies from 0 to 97.5 % w/w glycerol, yielding zero shear viscosities from 1 mPa s (for pure water (W)) to 813 mPa s (for 97.5 % w/w glycerol), densities from 1.05 g/ml to 1.25 g/ml, and an average surface tension of 65 mN/m, as measured with a pendant drop set-up.

The first viscoelastic system consists of bridged micro-emulsions composed of decane droplets of radius 6 nm^{14,40} stabilized in brine (0.2 M NaCl) by cetylpyridinium chloride (CpCl) as surfactant, and n-octanol as co-surfactant, with a molar ratio of n-octanol over CpCl of 0.65. The droplets are reversibly linked by polymer chains of poly(ethylene oxide) (PEO) of molar mass 35 kg/mol with hydrophobic stickers grafted at both ends, resulting in the formation of a transient network. The micro-emulsions are characterized by the number of carbon atoms in each sticker, n ($n = 12, 14$ or 18), the average number of stickers per droplet, r , comprised between 4 and 9, and ϕ , the mass fraction of oil

droplets ($\phi = 8, 10\%$). The sample preparation is described elsewhere¹³.

The second viscoelastic system consists of entangled wormlike micelles^{41,42} produced by self-organization, in 0.5 M brine, of surfactant molecules, sodium salicylate (NaSal) and CpCl, with a fixed molar ratio [NaSal]/[CpCl] of 0.5. Micelles are decorated by an amphiphilic polymer (*Synperonic F-108*), purchased from Serva, a PEO-PPO-PEO (with PPO being polypropylene oxide) triblock copolymer with an average molar mass of 14 kg/mol. The addition of amphiphilic polymer allows to easily tune the relaxation time⁴³. The micelles preparation is described in ref.⁴⁴. Micelles are characterized by ϕ , the mass fraction of surfactant (between 5 and 9%) and α the molar ratio of amphiphilic polymer over surfactant (from 0.48 to 4%).

Table 1 List of viscoelastic samples and their rheological properties. Micro-emulsion samples are named $Mn\phi XrY$ with n , the number of carbon per sticker for the telechelic polymers, X the value in % g/g for ϕ , the hydrophobic weight fraction and Y , the value of r , the average number of stickers per oil droplet. The name of wormlike micelle samples follows the nomenclature: $WM\phi X\alpha Y$ with X the value in % g/g for ϕ , the mass fraction of surfactant, and Y the value in % for α , the mole fraction of amphiphilic polymer. G_0 is the elastic modulus, τ , the relaxation time and $\eta_0 = G_0\tau$, the zero shear viscosity.

| Micro-emulsions | | | |
|---------------------------|------------|-------------|-----------------|
| Name | G_0 [Pa] | τ [ms] | η_0 [Pa s] |
| M18 ϕ 10r4 | 10 | 178 | 1.78 |
| M14 ϕ 8r9 | 189 | 8 | 1.5 |
| M14 ϕ 8r8 | 128 | 6 | 0.77 |
| M14 ϕ 10r6 | 48 | 5 | 0.23 |
| M14 ϕ 8r6 | 31 | 4 | 0.12 |
| M12 ϕ 10r8 | 194 | 2 | 0.39 |
| Wormlike micelles | | | |
| Name | G_0 [Pa] | τ [ms] | η_0 [Pa s] |
| WM ϕ 5 α 0.48 | 50 | 8 | 0.4 |
| WM ϕ 7 α 1.8 | 73 | 2 | 0.146 |
| WM ϕ 9 α 4 | 64 | 1 | 0.031 |

For both classes of viscoelastic samples, the linear rheological behavior can be well described in the frequency range of interest by a one mode Maxwell model in which the viscoelasticity is characterized by a single relaxation time, τ and a plateau modulus, G_0 . In this model, the storage and the loss moduli respectively read $G'(\omega) = \frac{G_0(\omega\tau)^2}{1+(\omega\tau)^2}$ and $G''(\omega) = \frac{G_0(\omega\tau)}{1+(\omega\tau)^2}$ with ω , the oscillation frequency. In reduced units, the storage and the loss moduli respectively read $\tilde{G}' = G'/G_0 = \frac{\tilde{\omega}^2}{1+\tilde{\omega}^2}$ and $\tilde{G}'' = G''/G_0 = \frac{\tilde{\omega}}{1+\tilde{\omega}^2}$ with $\tilde{\omega} = \omega\tau$. Fitting the frequency-dependent linear viscoelastic response of the samples with a Maxwell model allows one to determine the elastic plateau, G_0 and the characteristic time, τ . These characteristic parameters are reported in table 1 along with the dynamic viscosity, $\eta_0 = G_0\tau$ for all viscoelastic samples. The plateau modulus, G_0 , ranges from 10 to 194 Pa and the relaxation time, τ , from 1 ms to 178 ms, yielding dynamic viscosities, $G_0\tau$, between 0.031 and 1.78 Pa s. The samples are made to have relaxation times smaller than, comparable to, or larger than the characteristic time of the experiment, typically 6 ms, with the aim to probe viscous and elastic effects. We find (fig. 2) that the experimental data (symbols) for all viscoelastic samples collapse on one master curve which conforms to the one-mode Maxwell

model (lines), showing that the samples viscoelasticity can indeed be satisfyingly described by this model.

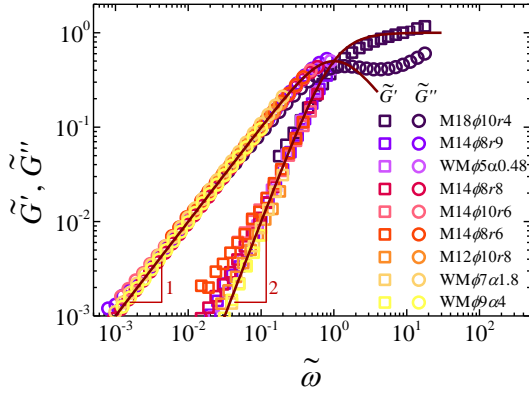


Fig. 2 (Symbols) Reduced storage, \tilde{G}' (squares), and loss, \tilde{G}'' (circles), moduli as a function of the reduced oscillatory frequency, $\tilde{\omega}$, for the viscoelastic samples, as indicated in the legend. Moduli, G' and G'' , are normalized by the sample shear modulus, G_0 , and the frequency, ω , is multiplied by the sample characteristic relaxation time, τ . (Lines) Theoretical expectations for a one-mode Maxwell fluid.

3 Experimental results

After its release, the drop reaches the surface covered with a thin liquid nitrogen layer and expands with a disk-like shape on a gaseous nitrogen cushion. After reaching a maximal expansion, the sheet retracts due to surface tension and bulk elastic energy. A series of snapshots showing the whole process, from the impact of the drop to the expansion of the sheet and subsequently its retraction is displayed in figure 3. The expansion and retraction events result in bell shaped curves for the time evolution of the diameter of the sheet. During the retraction regime, axisymmetry is lost due to non reversible instabilities and the sheet cannot be reasonably assimilated to a disk anymore. For this reason, this regime will not be further investigated. We define $\beta = \frac{d}{d_0}$, the stretching ratio with d , the apparent diameter of the sheet and d_0 , the initial diameter of the drop. The origin of time is chosen at the time at which the drop comes into contact with the nitrogen vapor layer in such a way that the diameter at $t = 0$ is d_0 , and hence $\beta = 1$. Figure 4a shows the time evolution of β for sample M14phi8r9 at different impact velocities, v_0 , from 1.5 to 5 m/s as indicated in the legend. The normalized diameter at maximum expansion, β_{\max} , increases monotonically with the impact velocity while the time to reach maximal expansion, t_{\max} , slightly increases with v_0 . Figure 4b shows the time evolution of β for all viscoelastic samples and three Newtonian samples with viscosity of 1, 216 and 658 mPa s, for a same impact velocity $v_0 = 4.2$ m/s. Overall, the curves follow the same general behavior but the key parameters, β_{\max} and t_{\max} , vary strongly from one sample to another (between 3.1 and 6.7 for β_{\max} and between 1.4 and 6.3 ms for t_{\max} at $v_0 = 4.2$ m/s) with no straightforward dependence on the rheological parameters, G_0 , τ or η_0 .

From the evolution of the diameter with time, we extract β_{\max} and t_{\max} . The viscoelastic fluids are impacted at different impact

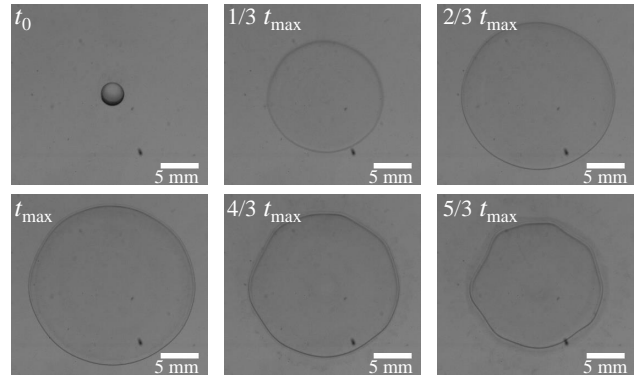


Fig. 3 Snapshots taken at different times, as indicated, during the expansion and retraction of a sheet produced with sample M14phi10r6 impacted at a velocity of 4.7 m/s. The bar sets the scale.

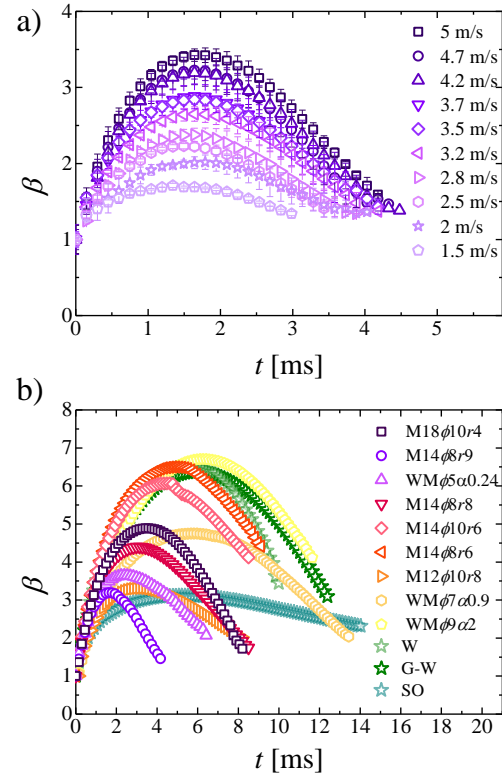


Fig. 4 Time evolution of the sheet diameter upon impact normalized by the initial drop diameter for (a) sample M14phi8r9 at different impact velocities as indicated in the legend (b) all viscoelastic samples and selected Newtonian fluids: pure water (W, $\eta_0 = 1$ mPa s), glycerol water mixture (G-W, $\eta_0 = 216$ mPa s) and silicone oil (SO, $\eta_0 = 658$ mPa s) impacted at $v_0 = 4.2$ m/s. The error bars in (a) represent the standard deviation of three different experiments. Error bars have been removed from (b) for more clarity.

velocities and the dependence of β_{\max} and t_{\max} with the impact velocity is shown in figures 5a,b. Additionally, the effect of v_0 on β_{\max} and t_{\max} for two Newtonian samples: water and a mixture with 91% g/g of glycerol in water ($\eta_0 = 216$ mPa s) is also shown in figures 5a,b. The other Newtonian samples (star symbols) are all impacted at one velocity ($v_0 = 4.2$ m/s) with β_{\max}

and t_{\max} decreasing for increasing viscosity (symbols of increasing darkness). The dependence of β_{\max} with the impact velocity follows $\beta_{\max} \propto v_0$ with prefactors which are sample-dependent. One could not infer simple correlations between the prefactors and the samples viscosity, bulk elasticity or relaxation time. On the other hand, t_{\max} is roughly constant with the impact velocity but varies from one sample to another. We observe a small decrease at low impact velocity for samples with relaxation time lower than the time of the experiment (M14 ϕ 8r8, M14 ϕ 10r6, M14 ϕ 8r6, M12 ϕ 10r8 and WM ϕ 7 α 1.8).

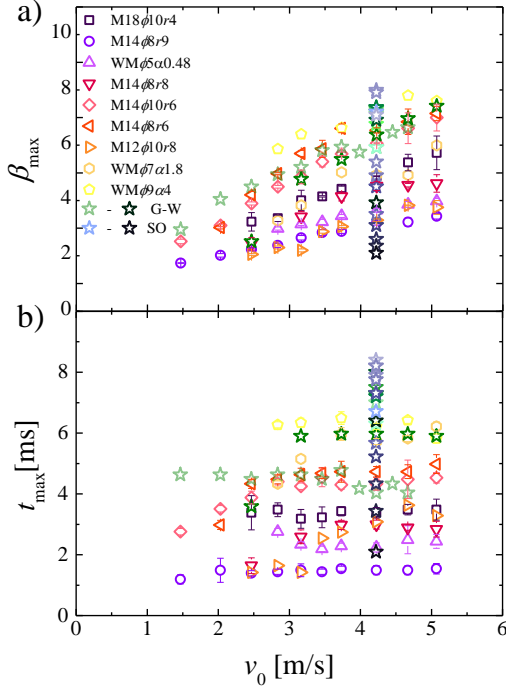


Fig. 5 Normalized maximal expansion (a) and time at maximal expansion (b) as a function of the impact velocity for all Newtonian and viscoelastic samples, as indicated in the legend. The increasing viscosity of the two classes of Newtonian samples are represented by shades of increasing darkness. The error bars represent the standard deviation of three different experiments.

The next section of the paper aims to predict the experimental values obtained for d_{\max} and t_{\max} by rationalizing the interplay between viscosity, and surface and bulk elasticity, for the expansion dynamic.

4 Damped oscillator model

4.1 Equation of motion

A common method to correlate the maximal stretching ratio, β_{\max} , to the impact parameters is to balance inertia with the energy contributions arising either from surface tension^{24,29,30}, bulk elasticity^{45,46} or both surface and bulk elasticity¹⁴. Below, we show that viscosity, surface tension and bulk elasticity are all crucial to quantitatively account for our experimental data. We write an energy balance equation for the expanding sheet after impact that includes at all times the contributions of the kinetic

energy, E_K , the surface energy, E_γ , the bulk elastic energy, E_{bulk} , and the biaxial extensional viscous dissipation energy, E_B .

$$E_K + E_\gamma + E_{\text{bulk}} + E_B = \text{Constant} \quad (1)$$

All energy terms are computed below considering the limit of large deformations ($d \gg d_0$) and assuming that the sheet, at all times, is a disk of diameter, d , and of uniform thickness, h_s ^{47,48}. From volume conservation, $h_s = \frac{2d_0^3}{3d^2}$.

The kinetic energy, E_K , reads

$$E_K = \int_0^{d/2} \frac{1}{2} v_r^2 \rho 2\pi h_s r dr = \frac{mv^2}{4} \quad (2)$$

with m , the mass of the drop, d , the diameter of the sheet at a time t and $v_r = \frac{2vr}{d}$, the Eulerian velocity field in the material along r , the radial coordinate, where v is the velocity of the expansion front. This velocity field has been found to describe accurately the expansion dynamics of Newtonian fluids^{10,49}.

The surface energy, E_γ reads

$$E_\gamma = \frac{1}{2} \pi \gamma d^2 \quad (3)$$

The contribution of the disk edge to the surface energy is neglected due to the large deformation limit considered here.

The bulk elastic energy, E_{bulk} , is approximated by the biaxial extensional linear elastic deformation energy of a soft solid in the limit of large deformation^{14,45}:

$$E_{\text{bulk}} \approx V_{\text{drop}} G_{\text{eff}} \left(\frac{d}{d_0} \right)^2 \quad (4)$$

with $V_{\text{drop}} = \frac{\pi d_0^3}{6}$, the volume of the drop and G_{eff} , the relevant shear elastic modulus of the sample, to be discussed in section 4.2.

We assume that the unique source of dissipation is viscous and originates from the biaxial extensional deformation of the sheet²⁸. Indeed, dissipation due to shear is eliminated thanks to the non wetting and slip conditions achieved with the cold Leidenfrost effect leaving biaxial extensional viscous dissipation as the only remaining viscous contribution. The biaxial extensional viscous dissipation energy, E_B , reads: $E_B = \int_0^{t_{\max}} \int_V \phi dV dt$. Here, ϕ is the dissipation function which reads $\phi \approx \eta_{B,\text{eff}} \dot{\epsilon}^2$ with $\dot{\epsilon} = \frac{1}{d} \frac{\partial d}{\partial t}$, the Hencky strain rate and $\eta_{B,\text{eff}}$, the relevant biaxial extensional viscosity of the sample. In the following, we assume $\eta_{B,\text{eff}}$ to be constant with time for one given impact experiment (i.e. one given sample and one given impact velocity)²⁸ as discussed in section 4.2.

$$E_B \approx \eta_{B,\text{eff}} \pi \frac{d_0^3}{6} \int_0^{t_{\max}} \left(\frac{1}{d} \frac{\partial d}{\partial t} \right)^2 dt \quad (5)$$

Inserting eqs.2-5 in the energy balance (eq.1) and deriving the latter with respect to time, one obtains the equation of motion for a free expanding sheet:

$$\ddot{d} + \frac{c(d)}{m} \dot{d} + \omega_0^2 d = 0 \quad (6)$$

Equation 6 is a non linear second order differential equation

that can be viewed as the equation of motion of a damped harmonic oscillator with an angular frequency:

$$\omega_0 = \sqrt{\frac{8\pi}{m} \left(\gamma + \frac{d_0 G_{\text{eff}}}{3} \right)} \quad (7)$$

and a non constant viscous damping coefficient which decreases through the expansion, as d increases.

$$c(d) = \frac{4\pi d_0^3 \eta_{\text{B,eff}}}{3} \frac{1}{d^2} \quad (8)$$

In the absence of viscous dissipation ($c = 0$) we retrieve the 1D undamped harmonic oscillator equation successfully used to model the expansion dynamics of sheets produced with various materials, with $\omega_0^2 = \frac{8\pi\gamma}{m}$ for Newtonian fluids of low viscosity²⁶ (in that case $G_{\text{eff}} = 0$), $\omega_0^2 = \frac{8\pi d_0 G_{\text{eff}}}{3m}$ for elastic beads⁴⁵ and $\omega_0^2 = \frac{8\pi}{m} \left(\gamma + \frac{d_0 G_{\text{eff}}}{3} \right)$ for ultrasoft elastic beads¹⁴. When viscous dissipation is not negligible, the relevant rheological parameters to consider are less straightforward, and are discussed below.

4.2 Discussion on the relevant rheological parameters

When viscous dissipation is not negligible, $c \neq 0$ is proportional to the biaxial extensional viscosity $\eta_{\text{B,eff}}$. In the case of Newtonian fluids ($G_{\text{eff}} = 0$), $\eta_{\text{B,eff}} = 6\eta_0$, the zero-shear viscosity multiplied by the Trouton ratio^{28,50}. The Newtonian sample biaxial extensional viscosities thus range from 6 to 4880 mPa s for mixtures of glycerol and water and from 30 to 5820 mPa s for silicone oil blends. For the Maxwell fluids, the approach is less straightforward as the biaxial extensional viscosity, but also the elastic modulus, are expected to be time-dependent to account for the samples viscoelasticity¹³. Hence, we need to estimate G_{eff} and $\eta_{\text{B,eff}}$ at the relevant frequency. As a first order approach, the relevant frequency can be estimated as the Hencky strain rate, $\dot{\epsilon}$, undergone by the sheet during its expansion. The Hencky strain rate is non-stationary and vanishes at maximal expansion as illustrated in figure 6a for one sample (M14 ϕ 8r9) impacted at different velocities. We choose as characteristic frequency the mean value of $\dot{\epsilon}$ averaged over the duration of the expansion regime: $\bar{\epsilon} = \frac{\int_0^{t_{\text{max}}} \dot{\epsilon} dt}{t_{\text{max}}}$. The mean values are plotted in figure 6b as a function of the impact velocity for all viscoelastic samples. We measure that $\bar{\epsilon}$ ranges between 194 and 516 s⁻¹ corresponding to Weissenberg number, $Wi = \bar{\epsilon}\tau$, values from 0.3 to 68.9. We find that $\bar{\epsilon}$ varies almost linearly with v_0 , with a sample-dependent proportionality constant. In the following, for Maxwell fluids, the relevant shear elastic modulus, G_{eff} , is taken as the elastic part, G' , of the complex modulus, G^* , at the relevant frequency:

$$G_{\text{eff}} = G'(\bar{\epsilon}) = G_0 \frac{(\tau \bar{\epsilon})^2}{1 + (\tau \bar{\epsilon})^2} \quad (9)$$

Similarly, the biaxial extensional viscosity for a viscoelastic fluids at the relevant strain rate is evaluated using the viscous part, G'' , of the complex modulus, G^* , and assuming the same Trouton ratio as for the Newtonian fluids:

$$\eta_{\text{B,eff}} = 6 \frac{G''(\bar{\epsilon})}{\bar{\epsilon}} = 6G_0 \frac{\tau}{1 + (\tau \bar{\epsilon})^2} \quad (10)$$

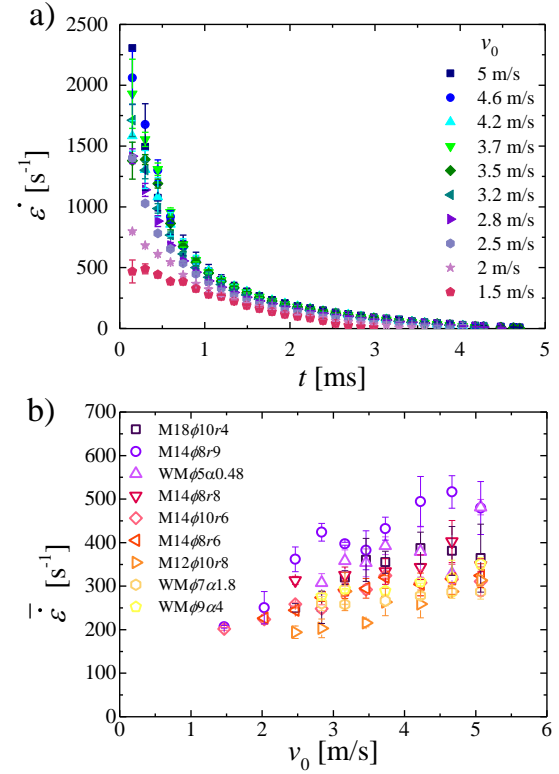


Fig. 6 (a) Time evolution of the Hencky strain rate during the sheet expansion for the sample M14 ϕ 8r9 at different impact velocities, v_0 , as indicated in the legend. (b) Strain rate averaged over time as a function of v_0 for all viscoelastic samples. Error bars represent the standard deviation of three different experiments.

4.3 Approximate analytical solution and comparison with experiments

Equation 6 is not analytically solvable. Therefore, we propose to solve the problem analytically for two limits of the damping coefficient: (i) $c \approx c_{\text{min}} = c(d_{\text{max}}) = \frac{4\eta_{\text{B}}\pi d_0^3}{3d_{\text{max}}^2}$ and (ii) $c \approx c_{\text{max}} = c(d_0) = \frac{4\eta_{\text{B}}\pi d_0}{3}$. In these two cases, the equation of motion of the free sheet (eq.6) reduces to a simple damped harmonic oscillator model with a constant damping factor. Using c_{max} , we overestimate the effect of the viscous drag and using c_{min} , we underestimate it. We check that all our samples verify the condition $\frac{c}{2m} < \omega_0^2$ which corresponds to the underdamped regime of the harmonic oscillator. In this regime, the solution of equation 6 is

$$d(t) = C e^{-\frac{c}{2m}t} \cos(\omega_d t - \Phi) \quad (11)$$

The parameters $\omega_d = \sqrt{\omega_0^2 - \left(\frac{c}{2m}\right)^2}$, $C = d_0 \sqrt{\left(\frac{2v_0}{d_0\omega_d} + \frac{c}{2m\omega_d}\right)^2 + 1}$ and $\Phi = \tan^{-1}\left(\frac{2v_0}{d_0\omega_d} + \frac{c}{2m\omega_d}\right)$ are obtained from the initial conditions, $d(0) = d_0$ and $\dot{d}(0) = 2v_0$ (See supplementary materials †). The maximum of d gives the theoretical time at maximal expansion which allows one to obtain the analytic equations, $t_{\text{max,a}}$ and $d_{\text{max,a}}$.

$$t_{\text{max,a}} = \frac{1}{\omega_d} \arctan\left(\frac{2v_0\omega_d}{d_0\omega_d^2 + \frac{c v_0}{m} + \frac{d_0 c^2}{4m^2}}\right) \quad (12)$$

$$d_{\max,a} = Ae^{-\frac{c}{2m}t_{\max,a}} \cos(\omega_d t_{\max,a} - \Phi) \quad (13)$$

In order to validate the present model, the analytical approximate predictions of the maximal diameter, $d_{\max,a}$ and the time at maximal expansion, $t_{\max,a}$ are compared with the experimental results. Figure 7 shows the experimental values for d_{\max} and t_{\max} plotted against the theoretical ones when using the relevant parameters of the drops in the underdamped harmonic oscillator model approximation (eqs.12, 13). In figure 7(a,b) the dissipation is evaluated with $c = c_{\min}$ and in figure 7(c, d) with $c = c_{\max}$. Lines representing $x=y$ allow one to judge more easily the quality of the analytical approximation of the model. The agreement between the underdamped harmonic oscillator model and the experimental data is good (relative error of approximately 30%). As expected, when the viscous dissipation is underestimated ($c = c_{\min}$), respectively overestimated ($c = c_{\max}$), overall the analytical predictions are larger (respectively smaller) than the experimental values and the data points are all below (respectively above) the lines $d_{\max,a} = d_{\max,exp}$ and $t_{\max,a} = t_{\max,exp}$.

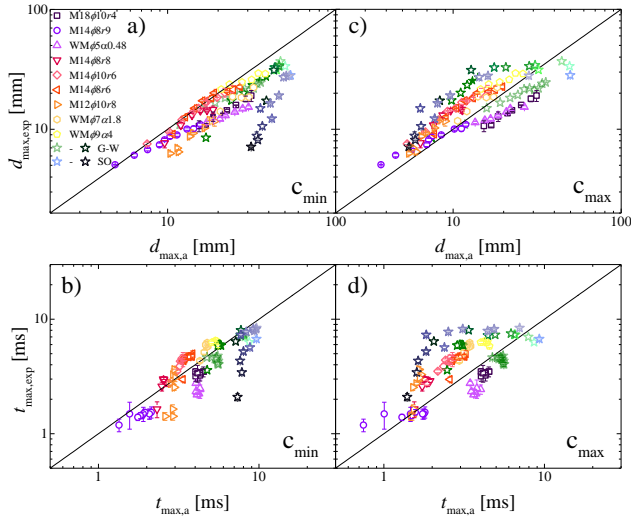


Fig. 7 Experimental d_{\max} (a, c) and t_{\max} (b, d) as a function of their respective theoretical predictions using the damped harmonic oscillator assumption with an underestimation (c_{\min} , a, b) or overestimation (c_{\max} , c, d) of the damping coefficient for all samples. The lines represent $x=y$.

4.4 Numerical resolution and comparison with experiments

To refine the prediction and better account for the competition between non-stationary elasticity, viscous dissipation and capillarity, we solve equation 6 numerically. Figure 8 shows the experimental data against the theoretical predictions after numerical resolution. The results agree well with the prediction for d_{\max} as well as for t_{\max} considering that no adjustable parameters are used to determine theoretical predictions. We can predict d_{\max} and t_{\max} with a relative error of approximately 25% for Newtonian fluids with biaxial extensional viscosities varying over three order of magnitude and viscoelastic samples spanning a large range of elastic moduli, characteristic relaxation times and viscosities. Despite the fact that we investigate Newtonian samples of high

viscosity and viscoelastic fluids, we find comparable relative error as previous works focusing on low viscosities Newtonian fluids impacted in similar conditions. Indeed, a relative error of 20%, at best, has been found when comparing experimental maximal expansion of Newtonian fluids of low viscosities impacted on a repellent surface⁵¹ to theoretical predictions using analytical, empirical, and scale relations^{52,53} as well as dynamical models⁵⁴⁻⁵⁶.

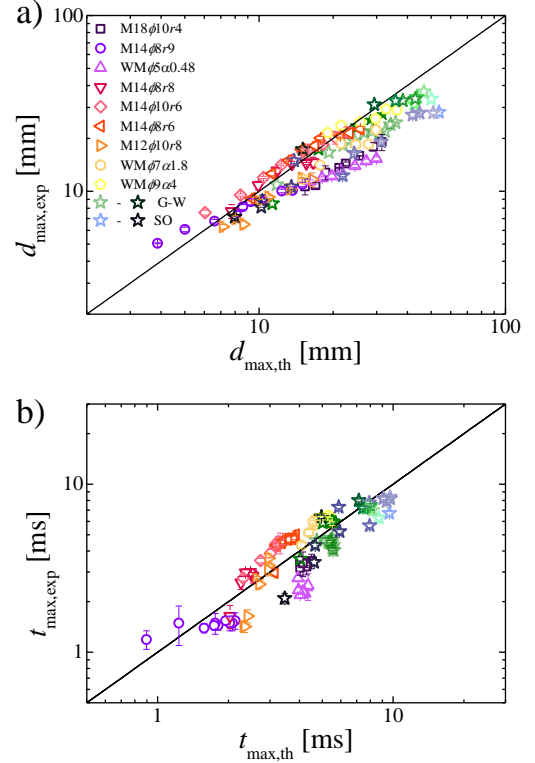


Fig. 8 Experimental (a) d_{\max} , and (b) t_{\max} as a function of their respective theoretical predictions using numerical resolution of equation 6 for all samples. The lines represent $x=y$.

Furthermore, the dynamics of expansion of the sheets can be relatively well described from only two parameters, t_{\max} and d_{\max} . Figure 9 shows, for four representative samples, the evolution of the experimental diameter (symbols) along with its numerical prediction using equation 6 (lines) normalized by their maximal values, as a function of the time normalized by t_{\max} . In the expansion regime, a maximal error of 5% is found between the normalized experimental data and the corresponding normalized theoretical predictions. Much larger deviations can be observed in the receding regime as different complex phenomena such as the loss of axisymmetry, expulsion of secondary droplets or pinning due to the cold surface, which are not taken into account in our rationalization, could occur.

5 Conclusion

Drop impact experiments on repellent surfaces have been performed with Newtonian and Maxwell fluids. Maxwell fluids have been carefully chosen to display a wide range of relaxation times, shorter, comparable or much larger than the typical experimental

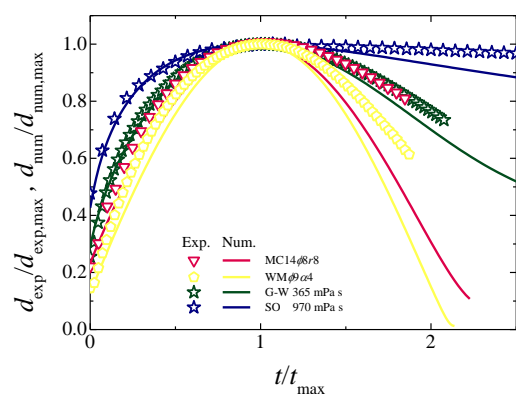


Fig. 9 Experimental (symbols) and theoretical (eq. 6) (lines) evolution of the diameter of the sheet normalized by its value at maximal expansion as a function of the time normalized by the time at maximal expansion for samples M14φ8r8 and WMφ9α4, a glycerol water mixture (G-W, $\eta_0 = 365$ mPa s) and a silicone oil (SO, $\eta_0 = 970$ mPa s) impacted at $v_0 = 4.2$ m/s.

time, allowing us to investigate the roles of viscosity, bulk elasticity and capillarity in the expansion dynamics of fluid sheets. We have used a cold Leidenfrost effect-based set-up so that the dominant source of viscous dissipation is the biaxial extensional deformation of the sheet. We have provided a systematic study of the effect of the impact velocity on the maximum diameter of the expanding sheet, and the time at which maximum expansion is reached. The expansion dynamics could be successfully modeled by a non linear damped harmonic oscillator model, where the damping coefficient decreases during the expansion and is proportional to the biaxial extensional dynamic viscosity, and the undamped angular frequency of the oscillator results from a simple combination of the surface tension and the dynamic modulus of the sample. For the viscoelastic samples, we have proposed to take as dynamic viscosity and dynamic modulus the viscosity and elastic modulus at a characteristic rate equal to the mean Hencky strain rate of the sheet in the expansion regime. The numerical prediction for the maximal expansion diameter, d_{\max} , and the time to reach maximal expansion, t_{\max} , agree quantitatively well with the experimental results, without adjustable parameters. Our approach is simple but quite general and we believe it could successfully be applied to more complex viscoelastic materials, of relevance for applications.

Conflicts of interest

There are no conflicts to declare.

Acknowledgements

This work was financially supported by the H2020 Program (Marie Curie Actions) of the European Commission's Innovative Training Networks (ITN) (H2020-MSCA-ITN-2017) under DoDyNet REA Grant Agreement (GA) N°.765811. We thank Pr. Daniel Read (University of Leeds) and Pr. Dimitris Vlassopoulos (IESL-FORTH) for fruitful discussions and Dr. Ty Phou (L2C,

Montpellier) for his technical assistance.

Notes and references

- 1 M. Pasandideh-Fard, V. Pershin, S. Chandra and J. Mostaghimi, *J. Therm. Spray Technol.*, 2002, **11**, 206–217.
- 2 W. Wirth, S. Storp and W. Jacobsen, *Pestic. Sci.*, 1991, **33**, 411–420.
- 3 N. Laan, K. G. De Bruin, D. Slenter, J. Wilhelm, M. Jermy and D. Bonn, *Sci. Rep.*, 2015, **5**, 11461.
- 4 H. Wijshoff, *Curr. Opin. Colloid Interface Sci.*, 2018, **36**, 20–27.
- 5 S. T. Thoroddsen, T. G. Etoh and K. Takehara, *Annu. Rev. Fluid Mech.*, 2008, **40**, 257–285.
- 6 C. Josserand and S. Thoroddsen, *Annu. Rev. Fluid Mech.*, 2016, **48**, 365–391.
- 7 Y. Wang and L. Bourouiba, *J. Fluid Mech.*, 2017, **814**, 510–534.
- 8 L. Gordillo, T. P. Sun and X. Cheng, *J. Fluid Mech.*, 2018, **840**, 190–214.
- 9 J. O. Marston, M. M. Mansoor and S. T. Thoroddsen, *Phys. Rev. E - Stat. Nonlinear, Soft Matter Phys.*, 2013, **88**, 1–4.
- 10 P. S. Raux, A. Troger, P. Jop and A. Sauret, *Physical Review Fluids*, 2020, **5**, 1–11.
- 11 F. Boyer, E. Sandoval-Nava, J. H. Snoeijer, J. F. Dijksman and D. Lohse, *Phys. Rev. Fluids*, 2016, **1**, 1–9.
- 12 R. Crooks and D. V. Boger, *J. Rheol.*, 2000, **44**, 973–996.
- 13 S. Arora, C. Ligoure and L. Ramos, *Phys. Rev. Fluids*, 2016, **1**, 1–15.
- 14 S. Arora, J. M. Fromental, S. Mora, T. Phou, L. Ramos and C. Ligoure, *Phys. Rev. Lett.*, 2018, **120**, 148003.
- 15 R. Rioboo, M. Marengo and C. Tropea, *Exp. Fluids*, 2002, **33**, 112–124.
- 16 M. Lee, Y. S. Chang and H.-Y. Kim, *Phys. Fluids*, 2010, **22**, 72101–72108.
- 17 M. Arogeti, E. Sher and T. Bar-Kohany, *Chem. Eng. Sci.*, 2019, **193**, 89–101.
- 18 A. L. N. Moreira, A. S. Moita, E. Cossali, M. Marengo and M. Santini, *Exp. Fluids*, 2007, **43**, 297–313.
- 19 Y. B. Wang, X. D. Wang, Y. R. Yang and M. Chen, *J. Phys. Chem. C*, 2019, **123**, 12841–12850.
- 20 Y. B. Wang, Y. F. Wang, S. R. Gao, Y. R. Yang, X. D. Wang and M. Chen, *Langmuir*, 2020, **36**, 9306–9316.
- 21 X. Wang, D. J. Lin, Y. B. Wang, S. R. Gao, Y. R. Yang and X. D. Wang, *AIChE J.*, 2020, **66**, e16647.
- 22 V. Bertola, *Adv. Colloid Interface Sci.*, 2013, **193–194**, 1–11.
- 23 P. Shah and M. M. Driscoll, *preprint arXiv:2012.10433*, 2020.
- 24 D. Richard, C. Clanet and D. Quéré, *Nature*, 2002, **417**, 811.
- 25 L. H. J. Wachters, L. Smulders, J. R. Vermeulen and K. HC, *Chem. Eng. Sci.*, 1966, **21**, 1231–1238.
- 26 A.-L. Biance, C. Clanet and D. Quéré, *Phys. Fluids*, 2003, **15**, 1632–1637.
- 27 C. Antonini, I. Bernagozzi, S. Jung, D. Poulikakos and M. Marengo, *Phys. Rev. Lett.*, 2013, **111**, 14501.

- 28 A. Louhichi, C.-A. Charles, T. Phou, D. Vlassopoulos, L. Ramos and C. Ligoure, *Phys. Rev. Fluids*, 2020, **5**, 053602.
- 29 A.-L. Biance, F. Chevy, C. Clanet, G. Lagubeau and D. Quéré, *J. Fluid Mech.*, 2006, **554**, 47–66.
- 30 M. Andrew, J. M. Yeomans and D. O. Pushkin, *Soft Matter*, 2017, **13**, 985–994.
- 31 Y. Tanaka, *Phys. Rev. E*, 2006, **73**, 31403–31406.
- 32 A. Jha, P. Chantelot, C. Clanet and D. Quéré, *Soft Matter*, 2020, **16**, 7270–7273.
- 33 S. Lin, B. Zhao, S. Zou, J. Guo, Z. Wei and L. Chen, *J. Colloid Interface Sci.*, 2018, **516**, 86–97.
- 34 D. Quéré, *Annu. Rev. Fluid Mech.*, 2013, **45**, 197–215.
- 35 S. Chen and V. Bertola, *Soft Matter*, 2016, **12**, 7624–7631.
- 36 K. J. Hendricks, R. C.; Baumeister, *NASA Technical Reports Server; NASA: Washington, DC*, 1970.
- 37 K. J. Hendricks, R. C.; Baumeister, *Advances in Cryogenic Engineering, Springer*, 1971, **16**, 455–466.
- 38 H. Kim, Y. H. Lee and H. Cho, *J. Korean Phys. Soc.*, 2011, **58**, 1628–1632.
- 39 A. Crisp, E. de Juan and J. Tiedeman, *Arch. Ophthalmol.*, 1987, **105**, 546–550.
- 40 M. Filali, M. J. Ouazzani, E. Michel, R. Aznar, G. Porte and J. Appell, *J. Phys. Chem. B*, 2001, **105**, 10528–10535.
- 41 H. Rehage and H. Hoffmann, *J. Phys. Chem.*, 1988, **92**, 4712–4719.
- 42 H. Rehage, & H. Hoffmann and H. Hoffmann, *Mol. Phys. An Int. J. Interface Between Chem. Phys. Mol. Physics*, 1991, **74**, 933–973.
- 43 G. Massiera, *Ph.D. thesis*, Université de Montpellier 2, 2002.
- 44 G. Massiera, L. Ramos and C. Ligoure, *Langmuir*, 2002, **18**, 5687–5694.
- 45 Y. Tanaka, Y. Yamazaki and K. Okumura, *Europhysics Lett.*, 2003, **63**, 146–152.
- 46 Y. Tanaka, *Eur. Phys. J. E*, 2005, **18**, 95–103.
- 47 P. Attané, F. Girard and V. Morin, *Physics of Fluids*, 2007, **19**, 012101.
- 48 J. Eggers, M. A. Fontelos, C. Josserand and S. Zaleski, *Phys. Fluids*, 2010, **22**, 1–13.
- 49 C. Vernay, L. Ramos and C. Ligoure, *Physical Review Letters*, 2015, **115**, 198302.
- 50 C. W. Macosko, *Rheology: Principles, Measurements and Applications*, Wiley-VCH, 1994.
- 51 J. T. Pearson, D. Maynes and B. W. Webb, *Exp. Fluids*, 2012, **53**, 603–618.
- 52 C. Clanet, C. Béguin, D. Richard and D. Quéré, *J. Fluid Mech.*, 2004, **517**, 199–208.
- 53 I. V. Roisman, *Phys. Fluids*, 2009, **21**, 052104.
- 54 M. Pasandideh-Fard, Y. M. Qiao, S. Chandra and J. Mostaghimi, *Phys. Fluids*, 1996, **8**, 650–659.
- 55 I. V. Roisman, R. Rioboo and C. Tropea, *Proc. R. Soc. A Math. Phys. Eng. Sci.*, 2002, **458**, 1411–1430.
- 56 C. Ukiwe and D. Y. Kwok, *Langmuir*, 2005, **21**, 666–673.